Fluorine atom abstraction by Si(100). I. Experimental

M. R. Tate, D. Gosalvez-Blanco, D. P. Pullman,[a] A. A. Tsekouras,[b] Y. L. Li, J. J. Yang, K. B. Laughlin, S. C. Eckman, M. F. Bertino, and S. T. Ceyer[c]
Department of Chemistry, Massachusetts Institute of Technology, Cambridge, Massachusetts 02139

(Received 16 March 1999; accepted 21 May 1999)

In the interaction of low energy F_2 with Si(100) at 250 K, a dissociative chemisorption mechanism called atom abstraction is identified in which only one of the F atoms is adsorbed while the other F atom is scattered into the gas phase. The dynamics of atom abstraction are characterized via time-of-flight measurements of the scattered F atoms. The F atoms are translationally hyperthermal but only carry a small fraction ($\sim$3%) of the tremendous exothermicity of the reaction. The angular distribution of F atoms is unusually broad for the product of an exothermic reaction. These results suggest an ''attractive'' interaction potential between F_2 and the Si dangling bond with a transition state that is not constrained geometrically. These results are in disagreement with the results of theoretical investigations implying that the available potential energy surfaces are inadequate to describe the dynamics of this gas–surface interaction. In addition to single atom abstraction, two atom adsorption, a mechanism analogous to classic dissociative chemisorption in which both F atoms are adsorbed onto the surface, is also observed. The absolute probability of the three scattering channels (single atom abstraction, two atom adsorption, and unreactive scattering) for an incident F_2 are determined as a function of F_2 exposure. The fluorine coverage is determined by integrating the reaction probabilities over F_2 exposure, and the reaction probabilities are recast as a function of fluorine coverage. Two atom adsorption is the dominant channel [$P_2=0.83\pm0.03(95\%,\ N=9)$] in the limit of zero coverage and decays monotonically to zero. Single atom abstraction is the minor channel ($P_1=0.13\pm0.03$) at low coverage but increases to a maximum ($P_1=0.35\pm0.08$) at about 0.5 monolayer (ML) coverage before decaying to zero. The reaction ceases at $0.94\pm0.11(95\%,\ N=9)$ ML. Thermal desorption and helium diffraction confirm that the dangling bonds are the abstraction and adsorption sites. No Si lattice bonds are broken, in contrast to speculation by other investigators that the reaction exothermicity causes lattice disorder.
 [S0021-9606(99)70431-9]

I. INTRODUCTION

Dissociative chemisorption is a fundamental step in the mechanism of chemical processes such as heterogeneous catalysis, chemical vapor deposition and semiconductor etching. The classic picture of dissociative chemisorption is cleavage of a bond between two atoms in a molecule incident on a surface concomitant with the formation of a bond between each of the atoms and the surface. The energy released in the formation of two bonds to the surface is necessary to compensate for the energy required to cleave the molecular bond. In contrast to classic dissociative chemisorption, cleavage of a molecular bond upon the formation of only a single bond to the surface is possible if the molecular bond energy is less than the energy released upon formation of the single bond to the surface. In this case, only one atom or fragment of the incident molecule remains adsorbed to the surface while the complementary atom or fragment is scattered into the gas phase. By analogy to gas phase abstraction reactions, this gas–surface mechanism is called atom abstraction. Phenomenologically, atom abstraction is the reciprocal process of the Eley–Rideal mechanism.[1] In the former case, the surface abstracts an atom from the incident molecule whereas in the latter case, the incident molecule abstracts an adsorbate from the surface.

Only recently has an experiment, which probed the interaction of F_2 with Si(100), conclusively demonstrated atom abstraction.[2] Despite extensive investigations of this particular important model system for semiconductor etching,[3,4] atom abstraction has not been reported.[5–7] The experimental difficulties are similar to those that precluded the direct observation of the Eley–Rideal mechanism until half a century after it was proposed.[8,9] In the case of atom abstraction, the observable is the atom or radical that is scattered into the gas phase. Because these scattered particles are highly reactive, they must be detected prior to their reaction with other surfaces (i.e., chamber walls) or gas phase species. This requirement necessitates an ultrahigh vacuum environment with sensitive, line-of-sight detection of the scattered products. Even though their detection is experimentally difficult, knowledge of the presence or even the plausibility of this mechanism is important from a practical standpoint because atom abstraction produces open shell atoms and radicals in the gas phase that may subsequently react in the gas phase or on other surfaces. The failure to properly account for these additional reactions in many applications may have signifi-

[a]Permanent address: Department of Chemistry, San Diego State University.
[b]Permanent address: Department of Chemistry, University of Athens.
[c]Electronic mail: stceyer@mit.edu

cant implications, not only for semiconductor etching but for such diverse applications as heterogeneous catalysis and chemical vapor deposition.

Of course, the fate of the complementary atom or fragment is not necessarily as a gas phase species. The scattered complementary species may subsequently interact with the surface of interest and if there is a reactive site near this interaction, it also may adsorb. Consequently, atom abstraction and the subsequent adsorption of the complementary species results in the formation of two surface–adsorbate bonds, just as in classic dissociative chemisorption. However, this process, called two atom adsorption, is distinct from classic dissociative chemisorption in that it is not a concerted process.[2] The fate of the complementary species is independent of the abstracted atom. The complementary species may adsorb on an adjacent site as in classic dissociative chemisorption or, after undergoing motion along the surface, it may adsorb on a nonadjacent site in contrast to classic dissociative chemisorption. It may also scatter back into the gas phase after undergoing motion along the surface.

Unlike the dearth of experimental results for atom abstraction, several theoretical investigations of the F_2/Si system have emphasized the atom abstraction mechanism. Stillinger and Weber (SW) developed one of the first potential energy hypersurfaces for the F_2/Si interaction using empirical two- and three-body potentials.[10] Their subsequent molecular dynamics simulations demonstrated the possibility of F atom abstraction. Weakliem, Wu, and Carter (WWC) modified the SW potential by incorporating *ab initio* results of the interaction of F with Si clusters, which enhanced the total reactivity of F and F_2 with Si.[11] Further simulations using the WWC potential probed the effects of incident translational and vibrational energy,[12] as well as steps and defects.[13] In addition, Garrison *et al.*[14] performed simulations on the interactions of F and F_2 with Si(100) using the WWC potential. The experimental observation of atom abstraction now provides the opportunity to test the accuracy of these potential energy surfaces.

This paper is the first of two papers[15] describing the interaction of low energy F_2 with Si(100) at 250 K. In the work presented here we focus on the initial event of the F_2/Si interaction, the F atom abstraction, with particular emphasis on the dynamics of the abstraction reaction at zero fluorine coverage and the quantitative determination of the saturation coverage. The experiment is carried out by scattering a F_2 beam from a Si(100) crystal and detecting the scattered reaction products, F and F_2, with a differentially pumped detector. In Sec. II we describe the experimental apparatus and the experimental method for determining the absolute flux of the incident F_2 molecular beam, a critical value in the quantitative analysis of this system. In Sec. III we present the evidence for atom abstraction, the velocity distributions of the scattered F and F_2 products as well as the dependence of the scattered products on F_2 exposure. It also presents the experimental results leading to the identification of the abstraction and adsorption sites. In Sec. IV we present a derivation of the absolute probability for single atom abstraction and two atom adsorption based on a quantitative analysis of the scattered products as a function of exposure. In addition, in this section we describe the determination of the absolute fluorine coverage as a function of F_2 exposure. In Sec. V we contrast the measured angular and velocity distributions of the scattered products and the experimentally measured branching ratio between the atom abstraction and two atom adsorption pathway to those predicted from simulations. The implications of these comparisons for the accuracy of the currently available potential energy surfaces for this system are discussed in detail. We also compare quantitatively the present results for the saturation coverage and for the total reactivity of F_2 with Si(100) with those measured previously. In the final part of the discussion, other gas–surface systems where atom abstraction may occur are considered.

In the second paper,[15] a model is presented that describes the kinetics of the interaction of F_2 with Si(100) over the entire range of possible fluorine coverages. Implications of this model for the microscopic dynamics of this gas–surface system as well as other related systems are discussed.

II. EXPERIMENT

The apparatus has been described in detail elsewhere.[16] Briefly, the apparatus consists of two differentially pumped, supersonic molecular beam sources coupled to an ultrahigh vacuum chamber (a base pressure of 5×10^{-11} Torr) containing the Si crystal, cylindrical mirror electrostatic energy analyzer for Auger spectroscopy, an ion sputtering gun, a residual gas mass analyzer and a triply differentially pumped, line-of-sight, rotatable quadrupole mass spectrometer.

A. Molecular fluorine beams

The molecular beams are skimmed and collimated through two differentially pumped regions. Expansion of 200 Torr of gas from a room temperature orifice of 0.003 in. diam typically yields a nearly monoenergetic beam ($\Delta E/E = 0.17$, $T = 10$ K) as measured by a time-of-flight (TOF) method. In these experiments, F_2 (97%, Air Products, subsequently purified through a HF trap, Matheson) is seeded (1%) in either Kr (99.997%, Spectra Gases) or Ar (99.9995%, Spectra Gases). The average translational energy (E_i) of F_2 in the resulting beams is 0.7 and 1.5 kcal/mol, respectively. At normal incidence, $\theta_i = 0°$, the beam illuminates a rectangular area with dimensions 0.250×0.177 in. positioned at the center of the 0.495 in. diam Si(100) crystal.

B. Determination of absolute flux of incident molecular beam

1. Single component molecular beam

Quantitative interpretation of the scattering data mandates an accurate value for the absolute flux of F_2 impinging on the Si surface.[17] The flux, I, of the beam impinging on an area, A, of the crystal is determined by measuring the change in the number density, N, of particles inside the main chamber upon introduction of the beam into it through a defining aperture. Assuming an ideal gas, the flux impinging on the crystal is

$$I=\frac{1}{A}\frac{dN}{dt}=\left(\frac{V}{kTA}\right)\left(\frac{dP}{dt}\right)+\left(\frac{P}{kTA}\right)\left(\frac{dV}{dt}\right), \tag{II.1}$$

where P, V and T are the pressure, volume and temperature, respectively, of the chamber. The time derivative of the volume, dV/dt, is the pumping speed, S, of the gas by the vacuum system. Two methods for measuring the number density change upon introduction of the beam are possible. Once the pressure in the main chamber is stabilized, the component of the steady state pressure, P, due to the beam is measured as the difference between the pressure after and before introduction of the beam. This value, along with the pumping speed, is used to calculate the flux from Eq. (II.1), where the first term is zero because P is constant in time. Alternatively, if the beam is allowed to enter the chamber when the pumps are isolated from it so that S and hence the second term are zero, the flux can be determined from Eq. (II.1) by measuring the rate of the pressure rise, dP/dt. Both methods have been examined and yield identical results to within 5%.[17] However, only the former method is discussed here.

At steady state, the flux at the surface is given by

$$I=\left(\frac{PCS}{kTA}\right). \tag{II.2}$$

The steady state pressure is measured with a nude Bayard–Alpert ionization gauge and is calibrated to the absolute pressure by accounting for the ionization efficiency, C, of the gas of interest. The ionization efficiency is determined by a comparison of the pressure reading from the ionization gauge to the absolute pressure of the gas. The absolute pressure is known from expansion of the gas from a small known volume ($\sim 10^{-3}$ L) at a pressure ($\sim$1–10 Torr), measurable by a capacitance manometer, into the large known volume ($\sim 10^{3}$ L) of the main chamber. The pumping speed, S, of the gas is determined by fitting the exponential function, $P=P_0\exp(-St/V)$, to the decaying partial pressure P of the gas, as measured by a mass spectrometer, upon abruptly terminating the beam. The chamber volume, V, has been determined both from gas expansions as well as from the design geometry. The temperature is measured by the thermocouple attached to the crystal in the absence of any cooling or heating. The exposed Si surface area, A, is determined both from the design geometry as well as the visible etch mark after months of exposure of the Si to F_2.

The flux of the incident F_2 beam would ordinarily be expressed in the number of F_2 molecules per unit time per unit area. However, in this application, a particularly well-suited unit for the flux impinging onto a single crystal surface is monolayers per second (ML/s), where a monolayer is defined as one F atom per Si surface atom. The number of Si atoms per unit area on the Si(100) surface is 6.78×10^{14} Si atoms/cm^2.

2. Absolute flux of a single component in seeded molecular beams

In principle, the F_2 flux onto the Si surface from a seeded F_2 beam can be estimated from the knowledge of the flux of a pure beam of the carrier gas and the nominal composition of the gas mixture before the expansion. However, after expansion of a 1% F_2/Kr mixture, Mach number focusing results in a higher concentration of Kr along the beamline than in the original mixture.[18–20] Therefore, the F_2 flux of the 1% F_2/Kr beam must be referenced to that of a beam which has negligible Mach number focusing. The coincidence of the masses of F_2 and Ar affords preparation of such a reference mixture, typically 1% F_2/Ar, whose F_2 flux can be determined from a measurement of the flux of a pure Ar beam, I_{Ar}, and from the nominal composition of the mixture. Accordingly, the F_2 flux from a 1% F_2/Ar beam, $I_{F_2/\mathrm{Ar}}$ is therefore $0.01\cdot I_{\mathrm{Ar}}$.

The F_2 flux in a mixture other than 1% F_2/Ar is determined by comparing the ion signals of F_2^+ in the mixture of interest with respect to that from the reference 1% F_2/Ar beam. The ion signal expected at a given charge-to-mass ratio, $m/e=M$, from a known particle flux I_M entering the mass spectrometer with velocity v_M is given by

$$S_M=\left(\frac{\sigma_{M\to M^+}I_{e^-}d_{e^-}T_M I_M}{v_M}\right), \tag{II.3}$$

where $\sigma_{M\to M^+}$ is the ionization cross-section, T_M is the transmissivity of ion M^+ through the quadrupole, I_{e^-} is the current density of bombarding electrons, and d_{e^-} is the length of the ionization region. The flux of electrons in the ionizer, expressed as the product of I_{e^-} and d_{e^-}, is independent of the m/e ratio and cancels in the ratio of any two F_2^+ signals. Although the ionization cross section and transmission function are dependent on the identity of the particle, the incident F_2 flux calculation only requires the F_2^+ signal and, therefore, these two factors also cancel in the ratio of any two signals. However, the ionization cross section and transmission function are necessary for the calculations presented in Sec. IV and are discussed in Sec. II D.

The ion signal is proportional to the ratio of the neutral particle flux and the neutral particle velocity because the detector measures number density, not flux. Thus, the ion signal must be weighted by the velocity to compare signals that arise from particles with different velocity distributions. The velocity-weighted counts (VWC) are determined by integrating the time-of-flight (TOF) signal, $f(t)$, weighted by the velocity or equivalently in time space by t^{-1},

$$\mathrm{VWC}=v_M S_M=\int_0^\infty t^{-1}f(t)\,dt. \tag{II.4}$$

The F_2 velocity-weighted counts, $\mathrm{VWC}_{F_2}^{F_2/\mathrm{Ar}}$ of the reference beam is determined from the integrated TOF signal at $m/e=38$ and used as a reference to compare against other F_2 seeded beams. In the case of the 1% F_2/Kr mixture used throughout the experiments, the F_2 flux is

$$I_{F_2/\mathrm{Kr}}=\left(\frac{\mathrm{VWC}_{F_2}^{F_2/\mathrm{Kr}}}{\mathrm{VWC}_{F_2}^{F_2/\mathrm{Ar}}}\right)I_{F_2/\mathrm{Ar}}, \tag{II.5}$$

where $\mathrm{VWC}_{F_2}^{F_2/\mathrm{mixture}}$ represents the velocity-weighted counts of F_2 measured from the integrated TOF signal at $m/e=38$ for the incident beam specified by the superscript. In the case of the reference beam, 1% F_2/Ar, the contribution to m/e

$=38$ from ^{38}Ar must be subtracted. It is determined from the integrated TOF signal of a pure Ar beam detected at $m/e=38$. The resulting F_2 flux is typically 0.366 ± 0.012 ML F atoms/s for the reference 1% F_2/Ar mixture and 0.170 ± 0.017 ML F atom/s for the 1% F_2/Kr mixture, where the uncertainties represent the propagated estimated errors or 95% confidence limits of the quantities in Eqs. (II.1)–(II.5). The F_2 flux of the 1% F_2/Kr beam is 0.68 of the nominal concentration, indicating the effect of Mach number focusing.[18]

C. Si(100) crystal

The crystal is mounted between two Ta clamps that are attached to the manipulator. The crystal normal can be rotated in the scattering plane defined by the axes of the two molecular beams and the detector. The axis of rotation is perpendicular to and intercepts the intersection of these three axes. The crystal can be cooled to 125 K and heated resistively to ~1100 K. Its temperature is measured via a W-5%Re/W-26%Re thermocouple spot welded to a thin Ta tab in thermal contact with the back of the crystal. The surface temperature is held constant at 250 K during F_2 exposure.

The Si crystal is cut along the (100) plane. Both lightly *n*-type and *p*-type doped Si with resistivities of 8–12 Ω cm have been used. No differences in reactivity have been observed for the two types of doping. The Si crystal is cleaned by a wet etching procedure[21] prior to installation into the vacuum chamber. The crystal is sputtered with 1.5 keV Ar^+ and subsequently annealed to about 1100 K. This process is repeated until C and O contamination are below the 1% sensitivity limit of Auger electron spectroscopy. No metal contamination, such as W, Ta, Cu, Ni, is observed. The crystal is typically mounted such that the scattering plane, defined by the beams, crystal normal and detector, is along the (10) direction of the crystal surface. Helium diffraction confirms the (2×1) periodicity of the reconstructed Si(100) surface. The crystal is sputtered and annealed each day to ensure surface cleanliness and order. A brief anneal of the crystal to about 1100 K after each F_2 exposure removes all the fluorine and results in the recovery of the (2×1) periodicity of the surface. The crystal is replaced when an etch spot becomes visible, typically after several months of experiments. No difference in reactivity is observed over the lifetime of the crystal. The results shown in this paper span many years and crystals.

D. Detection scheme

Primary measurements are made with a triply differentially pumped, rotatable quadrupole mass spectrometer with electron bombardment ionization. The detector rotates about the center point of intersection of the beam and the crystal. The angular range is 35°–180.3° with respect to the beam. The solid angle subtended by the detector is 5.8×10^{-4} sr. The angular resolution in the scattering plane is 3.52°. The rotation of the crystal and the detector allow for a wide range of incident and detection angles. A pseudorandom chopper wheel with 255 slots and spinning at 280 or 400 Hz at the entrance to the detector allows for measurements of the velocity distribution of both the incident beam as well as the scattered products using a cross correlation TOF technique. The neutral flight path is 29.3 ± 1.27 cm.

1. Determination of electron bombardment ionization cross sections

As discussed in Sec. IV, accurate values for the cross sections for electron bombardment ionization of F_2, $\sigma_{F_2\rightarrow F^+}$ and $\sigma_{F_2\rightarrow F_2^+}$ are necessary for a quantitative analysis of the data. Their values are determined by measuring their cross-sections relative to another particle whose absolute cross-section, $\sigma_{ref\rightarrow ref^+}$, is well known under similar ionization conditions. Using Eqs. (II.3) and (II.4), the equation for the cross section simplifies to

$$\sigma_{M\rightarrow M^+}=\left(\frac{\mathrm{VWC}_M}{\mathrm{VWC}_{\mathrm{ref}}}\right)\left(\frac{T_{\mathrm{ref}}}{T_M}\right)\left(\frac{I_{\mathrm{ref}}}{I_M}\right)\sigma_{\mathrm{ref}\rightarrow\mathrm{ref}^+}. \tag{II.6}$$

The most direct measurement of the $\sigma_{F_2\rightarrow F^+}$ cross section is obtained from TOF measurements of the 1% F_2/Ar reference mixture used to determine the absolute flux in Sec. II B 2. This mixture is chosen because the flux of the two components is well known and because the effects from Mach number focusing and quadrupole transmission are negligible. An absolute ionization cross section for Ar at 70 eV of $2.67\pm0.09\times10^{-16}\,\mathrm{cm}^2$ is used as a reference cross section.[22] Time-of-flight spectra are measured at $m/e=36$ ($^{36}Ar^+$) and $m/e=38$ (F_2^+); the ratio of these signals as defined by Eqs. (II.4) and (II.6) leads to the ionization cross section of interest,

$$\sigma_{F_2\rightarrow F_2^+}=\left(\frac{\mathrm{VWC}_{F_2}^{F_2/\mathrm{Ar}}}{\mathrm{VWC}_{36_{\mathrm{Ar}}}^{F_2/\mathrm{Ar}}}\right)\left(\frac{[^{36}\mathrm{Ar}]}{[F_2]}\right)\sigma_{\mathrm{Ar}\rightarrow\mathrm{Ar}^+}, \tag{II.7}$$

where I_{F_2} and $I_{^{36}Ar}$ simplify to their nominal concentrations in the seeded mixture, $[F_2]$ and $[^{36}Ar]$, since the 1% F_2/Ar beam exhibits no Mach number focusing. In addition, the velocities of the two components in the mixture are identical and therefore cancel. The ratio of transmissivities through the quadrupole is identical because the masses of F_2 and Ar are similar. The less abundant isotope, ^{36}Ar, is chosen so as to avoid the overwhelmingly large signal obtained from the measurement of the most abundant isotope, ^{40}Ar. The literature value[23] for the relative abundance of ^{36}Ar is used in determining $[^{36}Ar]$. As with the flux determination, the contribution of ^{38}Ar is subtracted from the F_2 signal.

Following similar arguments, the value of the velocity weighted counts at $m/e=19$ from a 1% F_2/Kr beam is used to determine the cross section $\sigma_{F_2\rightarrow F^+}$,

$$\sigma_{F_2\rightarrow F^+}=\left(\frac{\mathrm{VWC}_{19}^{F_2/\mathrm{Ar}}}{\mathrm{VWC}_{38}^{F_2/\mathrm{Ar}}}\right)\left(\frac{T_{38}}{T_{19}}\right)\sigma_{F_2\rightarrow F_2^+}, \tag{II.8}$$

where the concentrations in the seeded mixture cancel because the signals at $m/e=19$ and 38 come from the same neutral species. A Kr seeded beam is used to avoid the overlap of the F^+ signal ($m/e=19$) with the $^{38}Ar^{+2}$ signal

($m/e=19$) present in the 1% F_2/Ar beam. The transmission ratio T_{38}/T_{19} is determined as discussed below.

Values of $0.72\pm0.06\times10^{-16}\,cm^2$ and $0.28\pm0.06\times10^{-16}\,cm^2$ for $\sigma_{F_2\rightarrow F_2^+}$ and $\sigma_{F_2\rightarrow F^+}$, respectively, are obtained. The uncertainties represent the propagated 95% confidence limits of a minimum of 6 measurements and the estimated and given uncertainties of the quantities in Eqs. (II.7) and (II.8), respectively. The total ionization cross section for F_2, $1.00\pm0.08\times10^{-16}\,cm^2$, is the sum of the partial ionization cross sections and is in excellent agreement with a previously measured value of $1.1\times10^{-16}\,cm^2$.[24]

2. Determination of relative transmission through quadrupole

A critical value in the determination of the ionization cross sections in Eq. (II.8) is the relative transmissivity, T_{38}/T_{19}, of the $m/e=38$ and $m/e=19$ ions in the mass spectrometer. This value is determined by comparing the signal of two beams of known flux that contain species that ionize to the desired mass-to-charge ratios. Ar and Ne are chosen to obtain the transmissivity of Ar^+ and Ne^+ because of their similar masses to F_2 and F and because of the availability of accurate values for their absolute ionization cross sections.[22,25] Using Eqs. (II.3) and (II.4) for both Ar and Ne, the ratio of transmissivities is given by

$$\frac{T_{36}}{T_{22}}=\left(\frac{VWC_{36}^{Ar}}{VWC_{22}^{Ne}}\right)\left(\frac{\sigma_{Ne\rightarrow Ne^+}}{\sigma_{Ar\rightarrow Ar^+}}\right)\left(\frac{I_{22}Ne}{I_{36}Ar}\right), \tag{II.9}$$

where $\sigma_{Ar\rightarrow Ar^+}$ and $\sigma_{Ne\rightarrow Ne^+}$ are the electron impact ionization cross sections at 70 eV and where the fluxes appearing in the last factor are determined from the measured fluxes of the pure Ar and Ne beams weighted by their known natural isotope abundances.[23] The less abundant isotopic species, ^{36}Ar and ^{22}Ne, are monitored to ensure that the counting electronics are not saturated. On the assumption that a linear relationship between mass and transmissivity holds for this small mass range, the desired transmission ratio, T_{38}/T_{19}, is extrapolated from the measured value of T_{36}/T_{22} to be 1.00 ± 0.16, where the uncertainties represent the propagated 95% confidence limits of 6 measurements and the estimated and given uncertainties of the quantities in Eq. (II.9).

III. RESULTS

A. Identification of fluorine atom abstraction

In principle, F atom abstraction could be identified via observation of the scattered F atom, detected as F^+ ($m/e=19$). However, unreactively scattered F_2 molecules also contribute to the $m/e=19$ signal because they dissociatively ionize (or crack) to form F^+ in addition to ionizing to form F_2^+ ($m/e=38$) in the electron bombardment ionizer. The ratio of the F^+ signal to the F_2^+ signal measured by ionization of the incident F_2 beam by 70 eV electrons lies in the range 0.25–0.40, depending on the ionizer and quadrupole mass filter settings. This ratio is called the F^+/F_2^+ cracking ratio. While a discrepancy between this ratio and that of the F^+/F_2^+ signals of scattered F_2 might signal the production of F atoms by abstraction, the contributions of F atoms and F_2 molecules to the F^+ signal can be distinguished unambiguously by measuring the velocities with which the two particles scatter from the surface. The unreactive F_2 molecules ought to scatter with low velocity similar to their incident velocity of 395 m/s and the F^+ formed by dissociative ionization of this F_2 will have the same velocity. On the other hand, the F atoms scattered as products of atom abstraction and detected as F^+ ought to be translationally hot because of the exothermicity of the reaction. Figure 1(a) shows a superposition of such TOF spectra measured at $m/e=19$ and $m/e=38$ of F_2 at $E_i=0.7$ kcal/mol scattered from Si(100) at 250 K and integrated over a range of F_2 exposures, 0–1.9 ML F atom. The flight times are corrected for ion flight time and electronic delay. The $m/e=19$ distribution is distinctly bimodal with a narrow, fast feature and a broad, slow feature while the $m/e=38$ signal is comprised of a single slow feature. The $m/e=38$ signal is multiplied by the measured F^+/F_2^+ cracking ratio. The resulting absolute value of the $m/e=38$ signal represents the component of the $m/e=19$ signal resulting from dissociative ionization of F_2 and it matches well the intensity of the broad and slow feature of the $m/e=19$ signal. Therefore, the slow feature in the $m/e=19$ distribution arises from F^+ produced from the cracking of unreactively scattered F_2 whereas the narrow, fast feature arises from F atoms. Figure 1(b) shows the net scattered F atom signal obtained by subtracting the $m/e=38$ signal multiplied by the cracking ratio from the $m/e=19$ signal. The average velocity of scattered F atoms and F_2 is 1195 ± 57 m/s and 440 ± 20 m/s, respectively, where the major contribution to the uncertainties is the length of the flight path due to the finite length of the ionization region, 2.54 cm. The velocity distribution of the unreactively scattered F_2 is best fit by a

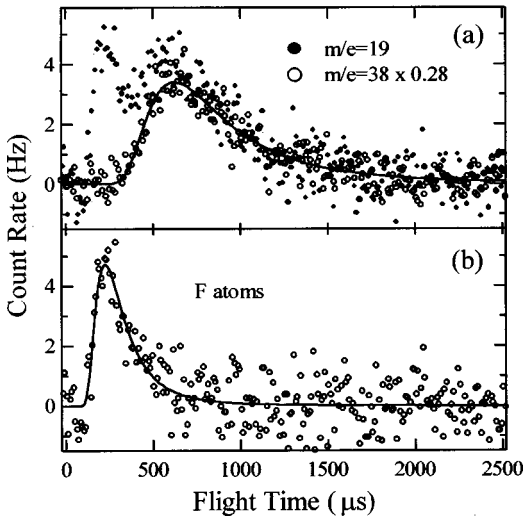

FIG. 1. (a) TOF spectra at $m/e=38$ multiplied by F_2 cracking ratio and at $m/e=19$ measured at $\theta_i=0°$, $\theta_d=35°$ and $T_s=250$ K. (b) Net scattered F atom TOF spectrum obtained by point-by-point subtraction of $m/e=38$ signal multiplied by the cracking ratio from the $m/e=19$ signal in (a). Solid lines show least squares fit of Maxwell–Boltzmann function $F(t)=Bt^{-4}\exp[-m(d/t-v)^2/2kT]$ for a number density distribution where t is flight time, d is flight length, T is beam temperature, m is mass and v is flow velocity. Spectra averaged over F_2 exposure of 0–1.9 ML F atom. Average velocities of corresponding flux distributions are $v_{F_2}=440\pm20$ and $v_F=1195\pm57$ m/s.

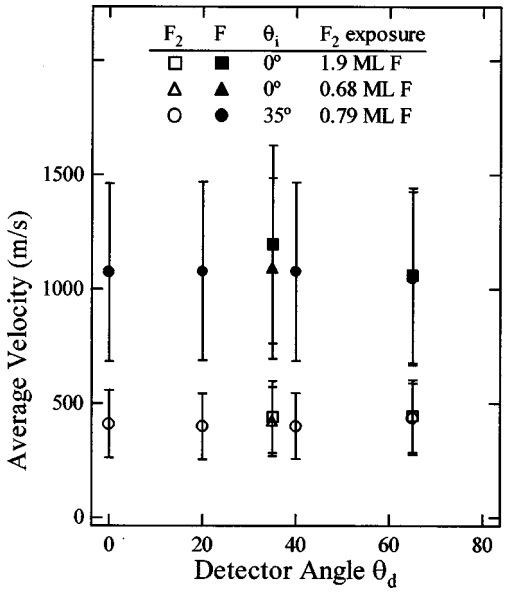

FIG. 2. Average velocity of scattered F atom and F_2 for a variety of scattering geometries and F_2 exposures at $E_i=0.7$ kcal/mol and $T_s=250$ K, determined from the fitting procedure identical to that in Fig. 1. Error bars represent full width at half of the maximum of velocity distributions. The uncertainty of the average velocity is typical of that in Fig. 1.

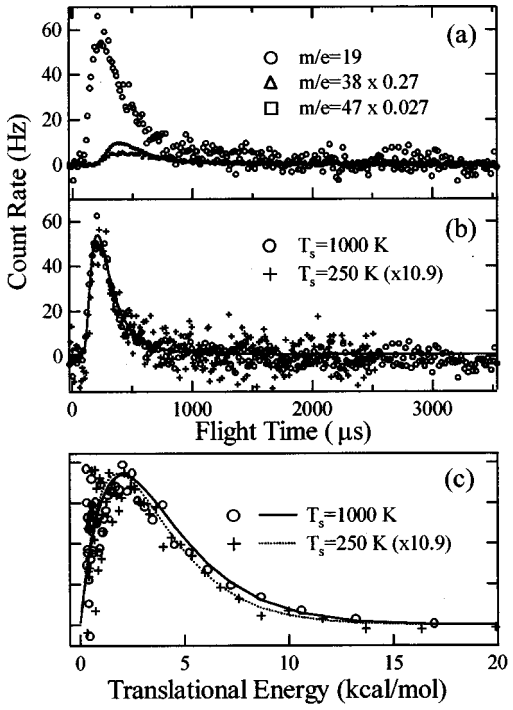

FIG. 3. (a) TOF spectra at $m/e=19$, $m/e=38$ and $m/e=47$ measured at $\theta_i=0°$, $\theta_d=35°$ and $T_s=1000$ K. Data at $m/e=38$ and $m/e=47$ multiplied by F_2 and SiF_2 cracking ratios, respectively. (b) Net scattered F atom TOF spectrum obtained by point-by-point subtraction of $m/e=38$ and $m/e=47$ signals multiplied by appropriate cracking ratios from the $m/e=19$ signal in (a). Net scattered F atom TOF spectrum at $T_s=250$ K, scaled by 10.9, is superimposed for comparison. Lines show a least squares fit as in Fig. 1. (c) Kinetic energy flux distributions of F atoms scattered from the surface at $T_s=250$ and 1000 K. Scaling factor of 10.9 determined by normalizing energy distributions at peak values.

Maxwell–Boltzmann distribution with a temperature of 248 K, essentially identical to the surface temperature of 250 K.

The TOF distributions shown here have been signal averaged over a wide range of F_2 exposure, 0–1.9 ML F, which corresponds to the entire range of fluorine coverage, 0–1 ML, as described in Sec. IV. Therefore, the TOF distributions could be artificially broadened if they were sensitive to the fluorine coverage. However, TOF distributions signal averaged over narrower ranges of F_2 exposure show that the F atom and F_2 velocity distributions are independent of exposure. The average velocities of some of these distributions are plotted in Fig. 2. The full widths at half of the maximum of the corresponding distributions are plotted as the error bars in Fig. 2. These results show that the dynamics of the interaction of F_2 with Si are insensitive to neighboring adsorbates.

Although the fast F atoms at $m/e=19$ that scatter from Si upon reaction with F_2 do not arise from the dissociation of unreactively scattered F_2 in the ionizer, there are other possible sources of the signal at $m/e=19$ to consider. For example, F atoms in the incident beam could survive the collision with Si and be scattered, but this possibility is highly unlikely because there is essentially no dissociation (10^{-8}%) of F_2 to F at 300 K and 200 Torr. The cracking of desorbing etch products (SiF_2, SiF_4, Si_2F_6) could yield a signal at $m/e=19$, but no species other than F, F_2 and Kr carrier gas are observed to scatter within the limit of the detection sensitivity of approximately 10^{10} particles/s or 10^{-5} ML/s. Finally, it is energetically possible for the F atoms produced as a result of atom abstraction to scatter from the surface as negative ions. This possibility was examined by placing a Faraday cup around the crystal, but no ions above the sensitivity limit of 10^{-7} ML/s were detected upon biasing either the cup or the crystal both positive or negative during exposure to the F_2 beam.

The results presented above are for a single scattering geometry in which the F_2 beam is at normal incidence to the surface, $\theta_i=0°$, and the detector is positioned at 35° from the normal to the surface, $\theta_d=35°$. Similar TOF measurements have been made at other detection angles as well as at $\theta_i=35°$ and other detection angles. Figure 2 shows the average velocities determined from these TOF measurements carried out for a variety of scattering geometries. These average velocities are independent of the scattering geometry. In addition, the velocity distributions from which these averages are determined are independent of the scattering geometry. Although these velocity distributions are not shown here, their full widths at half of the maximum are shown as the error bars in Fig. 2 and are observed to be independent of the scattering geometry.

To investigate the nature of the high translational energy of the F atoms, similar TOF measurements were made at a surface temperature of 1000 K. Figure 3(a) shows a superposition of TOF spectra measured at $m/e=19$, $m/e=38$, as well as $m/e=47$, which corresponds to SiF^+ arising from the dissociative ionization of the SiF_2 that desorbs at this high temperature during the exposure to F_2. The $m/e=38$ and $m/e=47$ signals are multiplied by the appropriate cracking ratios to represent the contributions of F_2 and SiF_2 to the F^+

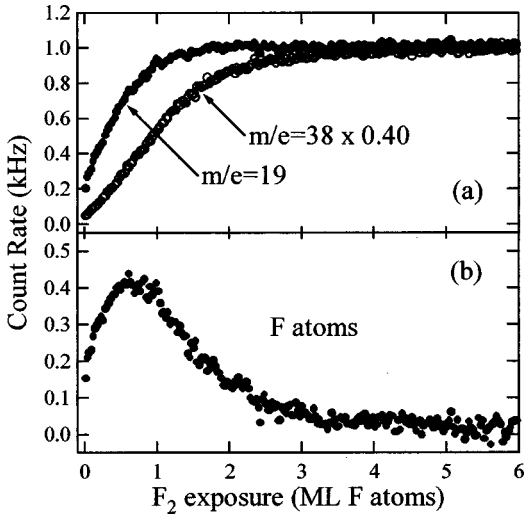

FIG. 4. (a) Signal at $m/e=19$ and $m/e=38$ multiplied by the F_2 cracking ratio as a function of F_2 exposure in ML F atom at $\theta_i=0°$, $\theta_d=35°$ and $T_s=250$ K. Signal is an average of 25 measurements. Statistical uncertainty is the size of data points. (b) Net scattered F signal calculated by point-by-point subtraction of the $m/e=38$ signal multiplied by the cracking ratio from the $m/e=19$ signal in (a).

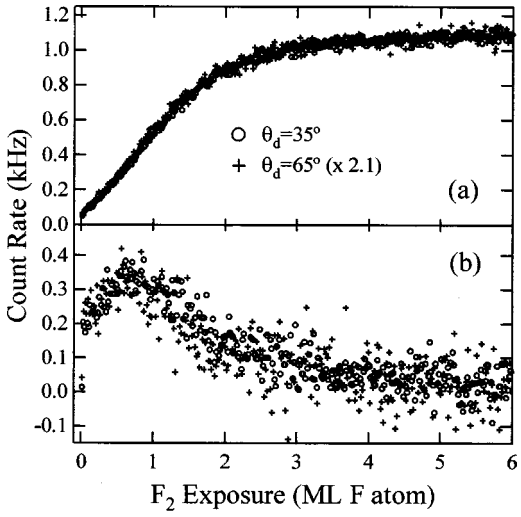

FIG. 5. (a) Signal at $m/e=38$ multiplied by the F_2 cracking ratio as a function of F_2 exposure at $\theta_i=0°$, $\theta_d=35°$ and $\theta_d=65°$. Scaling factor of 2.1 for $\theta_d=65°$ determined by matching its $m/e=38$ signal to that at $\theta_d=35°$ at long exposure. (b) Net scattered F signal at $\theta_d=35°$ and $\theta_d=65°$ calculated by point-by-point subtraction of the scaled $m/e=38$ signal multiplied by the cracking ratio from the scaled $m/e=19$ signal.

signal. Figure 3(b) shows the time distribution of the net scattered F atom signal obtained by subtracting the $m/e=38$ and $m/e=47$ signals multiplied by the appropriate cracking ratios from the $m/e=19$ signal. A scaled net F atom TOF distribution measured from a 250 K surface is superimposed for comparison, and it is seen to be nearly identical to the one measured at 1000 K. Figure 3(c) shows these distributions transformed into energy distributions, from which the average energies are calculated to be 3.7 ± 0.4 and 4.1 ± 0.4 kcal/mol at 250 and 1000 K, respectively. The insensitivity of these distributions to surface temperature demonstrates that the high translational energy of the F atoms is derived from the reaction exothermicity and not from the thermal motion of the surface atoms.

B. F atom abstraction as a function of exposure

In addition to direct identification of F atom abstraction, this investigation identifies the sites for abstraction and adsorption and determines the absolute probabilities for the three possible outcomes of the interaction of a F_2 molecule with a Si(100) surface: dissociative chemisorption via single atom abstraction, dissociative chemisorption via two atom adsorption and unreactive scattering. These probabilities are quantified in the limit of zero F coverage as well as for all F coverages up to the saturation coverage. These goals require that the exposure dependence of the scattered products be measured.

1. Exposure dependence of scattered products

The coverage dependence of the three reaction channels is contained in measurements of the scattered F and F_2, the products of atom abstraction and unreactive scattering, respectively, as a function of F_2 exposure. Figure 4(a) shows the signals at $m/e=19$ and $m/e=38$ as a function of F_2 exposure averaged over 25 exposures of the clean crystal to F_2. These two signals are collected almost simultaneously during a single F_2 exposure by switching the quadrupole mass filter between $m/e=19$ and $m/e=38$ at a rate of 10 Hz. The signal is collected beginning 5 ms after each switch to account for the finite switching time of the quadrupole power supply. The incident F_2 flux is low enough that the 5 Hz sampling rate per ion provides sufficient time resolution to observe the kinetics of the reaction. The $m/e=38$ signal in Fig. 4(a) is multiplied by the cracking ratio of F_2 to show the contribution of F_2 to the $m/e=19$ signal. Two observations are apparent. First, the $m/e=19$ and scaled $m/e=38$ signal levels are identical at long exposure. Thus, no F atoms are observed at long exposure, meaning that atom abstraction ceases at high coverage. Second, the $m/e=19$ and scaled $m/e=38$ signals evolve differently at low exposure. The larger signal at low exposure, $m/e=19$, arises from scattered F atoms as a consequence of atom abstraction. Figure 4(b) shows the net F atom signal as a function of exposure obtained by point-by-point subtraction of the $m/e=38$ signal multiplied by the cracking ratio of F_2 from the $m/e=19$ signal. The F atom signal, which is proportional to the probability of single atom abstraction, is low, but nonzero, at zero exposure, proceeds through a maximum at intermediate exposure and decays to zero at long exposure. A quantitative analysis of the exposure dependence of the scattered products is given in Sec. IV.

The exposure dependence of the scattered products described above is for a single scattering geometry, $\theta_i=0°$ and $\theta_d=35°$. Considering the hyperthermal velocity of the F atoms shown in Sec. III A, it is possible that the F atoms are anisotropically scattered. To investigate this possibility, the exposure dependence of the $m/e=19$ and $m/e=38$ signals was measured at $\theta_d=65°$ and is compared to that measured at $\theta_d=35°$ in Fig. 5. Figure 5(a) shows the $m/e=38$ signal at $\theta_d=65°$ multiplied by factor of 2.14. This factor is deter-

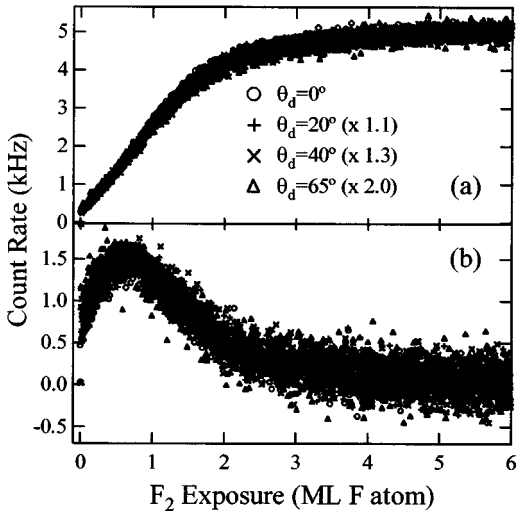

FIG. 6. (a) Signal at $m/e=38$ multiplied by the F_2 cracking ratio as a function of F_2 exposure at $\theta_i=35°$ and $\theta_d=0°$, 20°, 40° and 65°. Scaling factors determined by matching $m/e=38$ signals at long exposure as in Fig. 5. (b) Net scattered F signal at $\theta_d=0°$, 20°, 40° and 65° calculated as in Fig. 5.

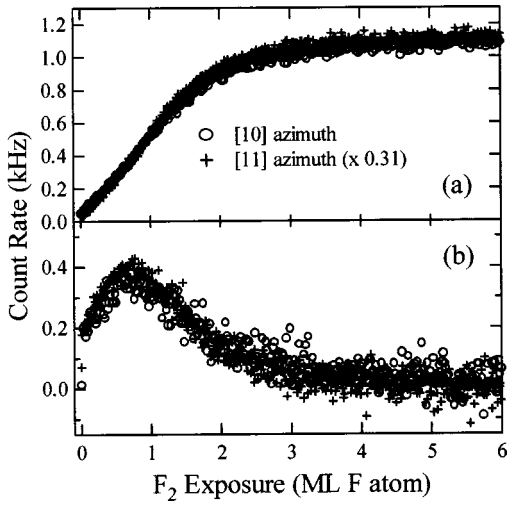

FIG. 7. (a) Signal at $m/e=38$ multiplied by the F_2 cracking ratio as a function of F_2 exposure at $\theta_i=0°$ and $\theta_d=35°$ for scattering along the (10) and (11) directions. Scaling factors determined by matching $m/e=38$ signals at long exposure as in Fig. 5. (b) Net scattered F signal for scattering along (10) and (11) directions calculated as in Fig. 5.

mined by requiring the $m/e=38$ signal at long exposure and at $\theta_d=65°$ to equal that at $\theta_d=35°$. As evident in Fig. 5(a), scaling the $m/e=38$ signal at $\theta_d=65°$ in such a manner allows the identicalness of the exposure dependence of the signals at the two detection angles to be easily seen in the regime of low exposure, where the probability of dissociative chemisorption of F_2 is not zero. Therefore, the angular distribution of the scattered F_2 does not change as the exposure increases. The net $m/e=19$ signal at $\theta_d=35°$ and that at $\theta_d=65°$ scaled by a factor of 2.14, both determined as described for the plot in Fig. 4(b), are shown in Fig. 5(b). The exposure dependence of the net $m/e=19$ signal at low exposures is again identical at the two detection angles, indicating that the angular distribution of the F atom signal does not change as the exposure increases. In addition, not only are the F atom and F_2 angular distributions independent of exposure, but the applicability of the same scale factor, 2.14, to both the F atom and the F_2 data, demonstrates that the F atom and the F_2 angular distributions are the same. The nature of the angular distributions is discussed in Sec. V.

Figures 6(a) and 6(b) show the exposure dependence of the $m/e=38$ and the net $m/e=19$ signals, respectively, measured at $\theta_i=35°$ and at four detection angles. The $m/e=38$ signals at $\theta_d=20°$, 40° and 65° are scaled to the $m/e=38$ signal at $\theta_d=0°$ and at long exposure, using the method described for the data in Fig. 5(a). The net $m/e=19$ signals are scaled by the factors determined in Fig. 6(a) using the method described for the data in Fig. 5(b). Again, the identicalness of the exposure dependence of the scaled signals and the applicability of the same scale factor to both the $m/e=38$ and the net $m/e=19$ signals indicates that the F_2 and F atom angular distributions do not vary with exposure and that the F_2 and F atom angular distributions are the same at $\theta_i=35°$.

The effect of the crystal's azimuthal orientation with respect to the scattering plane on the exposure dependence of the $m/e=38$ and $m/e=19$ signals was also examined. It is well known that orthogonal domains of (2×1) periodicity form on the Si(100) surface as a result of single steps created from even the slightest miscut of the crystal.[26] Therefore, scattering along the (10) direction actually samples scattering perpendicular to as well as parallel to the dimer rows. The experiments were repeated at $\theta_i=0°$ with the crystal azimuth rotated 45° such that scattering was along the (11) direction and at $\theta_d=35°$. The $m/e=38$ and net $m/e=19$ signals for this scattering geometry are shown in Figs. 7(a) and 7(b), scaled as described in Figs. 5 and 6 to the $m/e=38$ and net $m/e=19$ signals measured along the (10) azimuth and at $\theta_i=0°$ and $\theta_d=35°$. Note that the results for scattering along the (10) and (11) directions are identical. Thus, the interaction of F_2 with Si(100) is independent of the azimuthal angle, with no preferential scattering of the product along specific crystal axes.

The observation that the F_2 signal level attains a steady state implies that there is either a continuous constant reaction or no reaction at long exposure. Two observations already noted suggest that the reaction ceases and that F_2 merely passivates the Si surface. First, no etch products are observed to desorb. Therefore, if a continuous constant reaction were taking place, all F_2 that reacts would have to be continually incorporated onto or into the Si. A steady state reaction on a constantly changing surface is unlikely relative to a reaction that ceases when all of the reactive sites are occupied. Second, no F atoms are scattered in the steady state regime. As discussed below, single atom abstraction and two atom adsorption are related processes. It is unlikely that one process could cease while the other continues to occur. Thermal desorption and He diffraction measurements discussed in the following section are utilized to confirm that the interaction of low energy F_2 with Si at 250 K is a passivation reaction.

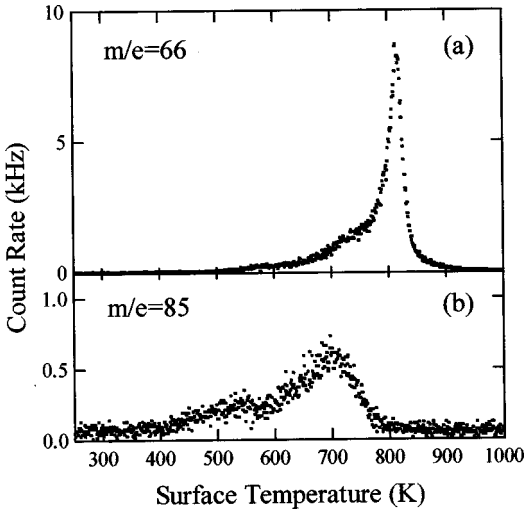

FIG. 8. Thermal desorption spectra at (a) $m/e=66$ and (b) $m/e=85$ after F_2 exposure of 19 ML F atom at $T_s=250$ K. Temperature ramp rate is 5 K/s.

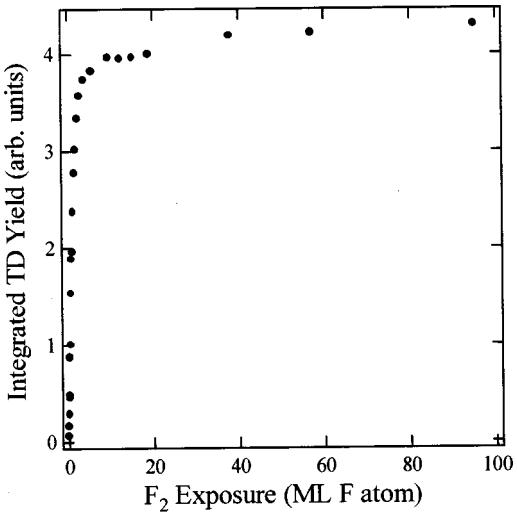

FIG. 9. Integrated thermal desorption yield as a function of F_2 exposure. The integrated signal at $m/e=85$ is scaled to correct for experimentally determined detection sensitivity of SiF_3^+ relative to SiF_2^+ as well as for the number of fluorine atoms per desorbing species.

2. Thermal desorption measurements

The crystal, at a temperature of 250 K, is exposed to F_2 at normal incidence, subsequently rotated so that the surface normal is along the axis of the triply differentially pumped mass spectrometer detector and then heated at a rate of 5 K/s from 250–1000 K. The desorption of multiple species is monitored essentially simultaneously by switching, at a rate of 10 Hz, the mass to which the quadrupole is tuned. Figure 8 shows thermal desorption spectra at $m/e=66$ and $m/e=85$ after a sufficiently long F_2 exposure to correspond to the steady state regime of Fig. 4. These two signals correspond to SiF_2^+ and SiF_3^+ and arise from SiF_2 and SiF_4, respectively. A comparison of the thermal desorption features at $m/e=66$ and 85, as well as at $m/e=104$, which corresponds to SiF_4^+ and is not shown, shows that there is no detectable SiF_3 contribution to the SiF_3^+ signal and no detectable SiF_4 contribution to the SiF_2^+ signal, in agreement with previous results.[27] The major thermal desorption product, SiF_2, is observed as a single feature centered around 800 K. The minor product, SiF_4, desorbs as two broad features around 550 and 700 K. The SiF_4 yield never exceeds 2.5% of the SiF_2 yield, even at F_2 exposures as large as 100 ML. The different velocity and angular distributions of the desorbing SiF_2 and SiF_4 species as well as their relative ionization cross sections and quadrupole transmissions are taken into account in this determination of their relative yield.[28]

The present interest in the thermal desorption measurements is to confirm that the reaction of F_2 with Si(100) ceases at long exposure when all of the reactive sites are occupied. Figure 9 shows the integrated thermal desorption yield as a function of F_2 exposure. The integrated yield is the sum of the integrated yields of SiF_2^+ and SiF_3^+ after scaling them for the relative detection sensitivities of the two signals and the factor of two more fluorine atoms that SiF_4 has relative to SiF_2. The integrated yield increases rapidly to a nearly steady state level. As determined in Sec. IV, the steady state level is achieved when the exposure is sufficiently high for the coverage to reach ~ 1 ML. However, careful inspection of Fig. 9 reveals that the integrated yield, and hence the coverage, is not exactly constant at very high F_2 exposures. Analysis and calibration of the slope of the plot of the integrated yield versus F_2 exposure beyond 20 ML F atom yields a value of 9×10^{-4} for the dissociative chemisorption probability of F_2 on a Si(100) surface covered with about 1 ML of fluorine.[28] However, for all intents and purposes, the steady state regime corresponds to a cessation of adsorption of F_2 on Si(100) as opposed to a continual adsorption reaction that has achieved a steady state.

It should be noted that the thermal desorption spectrum of SiF_3^+ observed in this work does not agree with that of a previous study in which an additional SiF_3^+ feature around 800 K was observed.[6] To confirm that the additional SiF_3^+ feature is an artifact that resulted from the use of a mass spectrometer without differential pumping,[6] both the SiF_3^+ and the SiF_2^+ spectra were remeasured with an undifferentially pumped mass spectrometer that resides in the same chamber as the crystal and are shown in Fig. 10. The SiF_3^+ spectrum indeed exhibits an additional feature whose desorption temperature around 800 K matches well with that of the SiF_2^+ desorption feature. These observations demonstrate that this additional SiF_3^+ signal arises from the SiF_4 produced by the reaction of SiF_2 with the fluorinated chamber walls. A comparison of the results in Figs. 8 and 10 illustrates how spurious features due to secondary interactions of the desorbing species, particularly a radical species such as SiF_2, with the chamber walls or in the gas phase are eliminated with proper differential pumping of the detector.

3. Helium diffraction

Si(100) reconstructs forming rows of surface Si dimers resulting in one partially-filled molecular orbital or dangling bond projecting into the vacuum for each surface Si atom and yielding a (2×1) periodicity that is observable by He diffraction.[26] These dangling bonds, which effectively are radical sites and hence very reactive species, are logical sites

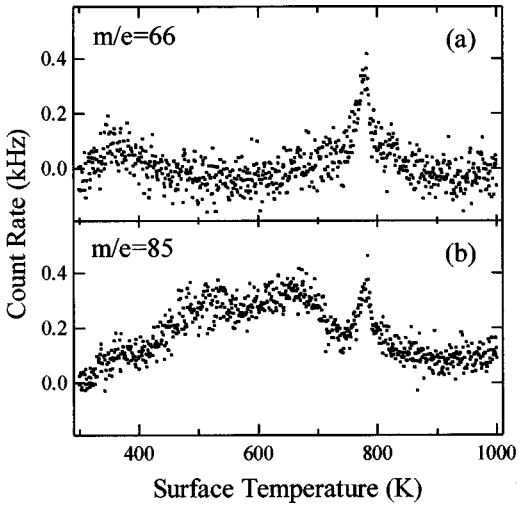

FIG. 10. Thermal desorption spectra at (a) $m/e=66$ and (b) $m/e=85$ under same conditions as in Fig. 8 except measured with nondifferentially pumped mass spectrometer with crystal facing away from the spectrometer.

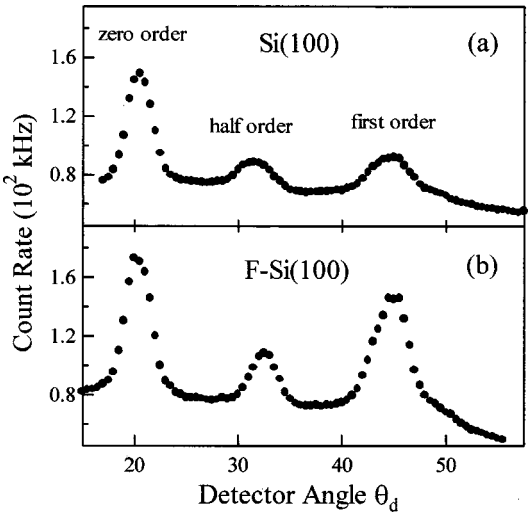

FIG. 11. Helium signal scattered from Si(100) at 250 K and at $\theta_i=20°$ as a function of θ_d: (a) clean surface: (b) after F_2 exposure of 30 ML F atom.

for F atom abstraction and adsorption. The goal here is to identify the site of F adsorption as well as to determine the extent of Si–Si bond cleavage, if any. While He diffraction cannot directly identify the F adsorption site, it can reveal the prevailing periodicity to determine which periodic structures have been disrupted upon F adsorption, thereby providing supporting evidence for the dangling bonds as the F atom adsorption sites in the interaction of F_2 with Si(100)2×1.

A mixture of He seeded in Ar is expanded to produce a He beam that has an average velocity and temperature of 766 ± 65(FWHM) m/s and 2 K, respectively, as determined from TOF measurements. The average wavelength of the incident He is 1.31 ± 0.11(FWHM) Å, which is comparable to the surface unit cell dimensions of 3.84 Å and 7.68 Å. The beam is incident at $\theta_i=20°$ and is modulated at 150 Hz with a tuning fork to allow for background subtraction. The detector is rotated in steps of 0.5° from 15°–55° with respect to the surface normal in the forward scattering direction. Figure 11(a) shows a plot of the scattered He intensity as a function of the scattering angle, θ_d, measured from the surface normal of a clean Si(100) surface at 250 K. The features are broad because of the low angular resolution of the detector that is necessary to obtain sufficient sensitivity to detect reactive species which typically scatter with very low fluxes.[16] However, three primary features of the diffraction spectrum indicative of the (2×1) periodicity are apparent. These features are a specular peak arising from overall order and smoothness, a half order peak at $\theta_d=31°$ arising from diffraction perpendicular to the dimer rows and a first order peak at $\theta_d=43°$ arising from diffraction parallel to the dimer rows. Figure 11(b) shows He diffraction from a Si(100) surface at 250 K after a sufficiently long exposure to F_2 so as to reach the steady state regime of Figs. 4 and 9. Although the intensities of the features are changed upon fluorination, the (2×1) periodicity persists. The identical two-dimensional unit cells of the fluorine overlayer and the Si(100) surface strongly suggests that each dangling bond serves as an adsorption site for one F atom. More importantly, the persistence of the half order feature indicates that no Si lattice bonds, not even the σ Si dimer bonds, are broken upon reaction with F_2. There is no etching of the Si surface nor is the surface disordered upon reaction with F_2.

The thermal desorption and He diffraction results along with the quantitative determination of the saturation coverage carried out in the next section will be used to confirm that the reaction proceeds via adsorption on the Si dangling bonds. When all of the dangling bonds have been fluorinated, the reaction stops.

IV. ANALYSIS

In this section we present a quantitative analysis of the dependence of the amount of F and F_2 scattered from Si(100) on F_2 exposure, yielding the absolute reaction probabilities as a function of fluorine coverage. The saturation coverage is established to be 1 ML, confirming that F_2 simply decorates the highly reactive Si dangling bonds and does not break the Si dimer bonds.

A. Dependence of the reaction probabilities of F_2 with Si(100) on F_2 exposure

The scattering of a F_2 molecule from Si(100) follows one of three possible channels.

Unreactive scattering (P_0) is the channel in which F_2 scatters intact from the surface into the gas phase where it is detected as either F_2^+ or F^+. The absence of F_2 adsorption at long exposures demonstrated by the thermal desorption measurements means that only unreactive scattering occurs at long exposures to F_2. Therefore, at long exposure, $\epsilon=\infty$, the flux of unreactively scattered F_2 is equal to the incident flux of F_2. Thus, the absolute probability for unreactive scattering, P_0, as a function of F_2 exposure, ϵ, is the ratio of the scattered F_2 flux at ϵ to the scattered F_2 flux at $\epsilon=\infty$:

$$P_0(\epsilon)=\frac{\text{scattered } F_2 \text{ flux}}{\text{incident } F_2 \text{ flux}}=\frac{I_{F_2}^{\text{scat}}(\epsilon)}{I_{F_2}^{\text{scat}}(\infty)}. \tag{IV.1}$$

Single atom abstraction (P_1) is the channel in which one of the F atoms is adsorbed onto the surface while the complementary F atom scatters into the gas phase and is detected as F^+. The absolute probability for single atom abstraction, P_1, as a function of ϵ is again determined by referencing the F atom flux to the scattered F_2 flux at long exposure and is given by

$$P_1(\epsilon)=\frac{\text{scattered F flux}}{\text{incident } F_2 \text{ flux}}=\frac{I_F^{scat}(\epsilon)}{I_{F_2}^{scat}(\infty)}. \tag{IV.2}$$

Two atom adsorption (P_2) is the channel in which both fluorine atoms of F_2 are adsorbed onto the surface and no scattered products are detected in the gas phase. Normalization of the three channels yields the absolute probability for two atom adsorption, P_2, given by

$$P_2(\epsilon)=1-P_0(\epsilon)-P_1(\epsilon). \tag{IV.3}$$

In order to calculate these probabilities, expressions for the scattered F_2 and F fluxes, $I_{F_2}^{scat}$ and I_F^{scat}, respectively, in terms of the measurable quantity, the signal detected by the mass spectrometer, must be obtained. The mass spectrometer signal collected at a scattering angle, θ_d, is proportional to the number density of ions produced at $m/e=38$ and $m/e=19$ upon ionization of the neutral products, F_2 and F, and are related to the scattered fluxes at θ_d by

$$S_{38}(\epsilon,\theta_d)=\frac{I_{F_2}^{scat}(\epsilon,\theta_d)\sigma_{F_2\rightarrow F_2^+}T_{38}}{v_{F_2}} \tag{IV.4}$$

and

$$S_{19}(\epsilon,\theta_d)=\frac{I_{F_2}^{scat}(\epsilon,\theta_d)\sigma_{F_2\rightarrow F^+}T_{19}}{v_{F_2}}+\frac{I_F^{scat}(\epsilon,\theta_d)\sigma_{F\rightarrow F^+}T_{19}}{v_F}, \tag{IV.5}$$

where $S(\epsilon,\theta_d)$ is the exposure and detector angle dependent signal at m/e denoted by its subscript, σ is the appropriate electron-impact ionization cross section at the electron energy used for the measurement, v is the average velocity of the scattered neutral indicated by its subscript and T is the transmissivity of the ion through the quadrupole mass filter at m/e denoted by its subscript. A proportionality factor, composed of the product of the current density of bombarding electrons in the ionizer and the length of the ionization region is not included in Eqs. (IV.4) and (IV.5) because these instrument quantities are independent of the particles' identity and cancel in the ratios used to define the probabilities in Eqs. (IV.1)–(IV.3). Equation (IV.5) shows that there are two contributions to the signal at $m/e=19$. The first contribution comes from the dissociative ionization of F_2 in the ionizer while the second arises from the ionization of scattered F atoms.

Solving Eq. (IV.4) for the scattered F_2 flux, $I_{F_2}^{scat}$, yields

$$I_{F_2}^{scat}(\epsilon,\theta_d)=\frac{S_{38}(\epsilon,\theta_d)v_{F_2}}{\sigma_{F_2\rightarrow F_2^+}T_{38}}. \tag{IV.6}$$

This result is substituted into Eq. (IV.5), which can then be solved for the scattered F atom flux I_F^{scat}:

$$I_F^{scat}(\epsilon,\theta_d)=\left(S_{19}(\epsilon,\theta_d)-\left(\frac{\sigma_{F_2\rightarrow F^+}T_{19}}{\sigma_{F_2\rightarrow F_2^+}T_{38}}\right)S_{38}(\epsilon,\theta_d)\right)\times\left(\frac{v_F}{\sigma_{F\rightarrow F^+}T_{19}}\right). \tag{IV.7}$$

Using Eq. (IV.1), the probability for unreactive scattering at a scattering angle θ_d, $P_0(\epsilon,\theta_d)$, can now be written in terms of the experimentally measured quantity, $S_{38}(\epsilon,\theta_d)$, such as presented in Fig. 4. Because the F_2 velocity distribution is independent of exposure as discussed in Sec. III A, $P_0(\epsilon,\theta_d)$ simplifies to

$$P_0(\epsilon,\theta_d)=\frac{S_{38}(\epsilon,\theta_d)}{S_{38}(\infty,\theta_d)}. \tag{IV.8}$$

Using Eq. (IV.2), an expression for $P_1(\epsilon,\theta_d)$ is written as the ratio of Eq. (IV.7) to Eq. (IV.6) evaluated in the limit of infinite exposure,

$$P_1(\epsilon,\theta_d)=\left(\frac{v_F}{v_{F_2}}\right)\left(\frac{\sigma_{F_2\rightarrow F_2^+}}{\sigma_{F\rightarrow F^+}}\right)\left(\frac{T_{38}}{T_{19}}\right)\left(\frac{1}{S_{38}(\infty,\theta_d)}\right)\times\left(S_{19}(\epsilon,\theta_d)-S_{38}(\epsilon,\theta_d)\left(\frac{\sigma_{F_2\rightarrow F^+}T_{19}}{\sigma_{F_2\rightarrow F_2^+}T_{38}}\right)\right). \tag{IV.9}$$

The ratio in the last term is the cracking ratio of F_2. Therefore, the difference term is the signal at $m/e=19$ arising from F atoms. After some algebra, the ratio of transmissivities can be eliminated yielding the final form for P_1:

$$P_1(\epsilon,\theta_d)=\left(\frac{v_F}{v_{F_2}}\right)\left(\frac{\sigma_{F_2\rightarrow F^+}}{\sigma_{F\rightarrow F^+}}\right)\left(\frac{S_{19}(\epsilon,\theta_d)}{S_{19}(\infty,\theta_d)}-\frac{S_{38}(\epsilon,\theta_d)}{S_{38}(\infty,\theta_d)}\right). \tag{IV.10}$$

The assumption is made that only F_2 contributes to the F^+ signal at long exposure. All quantities except for $\sigma_{F\rightarrow F^+}$ can be measured with the apparatus described in Sec. II. The F and F_2 velocities are average values of the average velocities plotted in Fig. 2, 1084 ± 46 and 419 ± 18 (95%, $N=7$) m/s, respectively. Recall that both velocities were shown to be independent of exposure. The ionization cross section of F_2 to F^+, $\sigma_{F_2\rightarrow F^+}$, is 0.28 ± 0.06 Å^2 as measured by the method presented in Sec. II. A literature value, 0.87 ± 0.17 Å^2, is used as the F atom ionization cross section, $\sigma_{F\rightarrow F^+}$, at 70 eV electron energy.[29] The final term is simply the difference between the two scattered signals normalized to their respective steady state levels at long exposures. Once P_0 and P_1 have been obtained, P_2 follows by the normalization condition expressed in Eq. (IV.3). The F_2 exposure is determined from the absolute flux of the incident beam. Figures 12(a)–12(c) show the probabilities of the three channels as a function of F_2 exposure at $\theta_d=35°$. The error bars represent the propagated uncertainties of the quantities in Eqs. (IV.8) and (IV.10) typical of a single data set. The large uncertainty in the determination of P_1 results from the uncertainty in the literature value of $\sigma_{F\rightarrow F^+}$ whose relative error is 20%.[29]

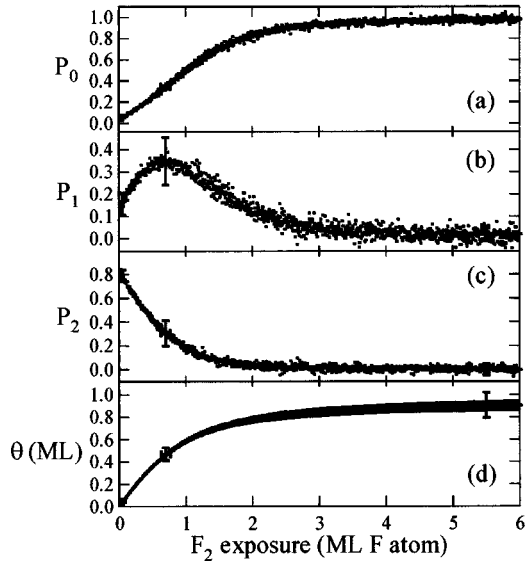

FIG. 12. Reaction probability of F_2 with Si(100) as a function of F_2 exposure for (a) unreactive scattering P_0, (b) single atom abstraction P_1, (c) two atom adsorption P_2. Six data sets collected over a period of two months using two different crystals are shown. Each data set is typical of that in Fig. 4. Error bars on P are propagated uncertainties typical of a single data set. Error bars on exposure reflect uncertainty in beam flux. (d) Absolute fluorine coverage as a function of F_2 exposure in ML F atom. Error bars on coverage reflect propagated uncertainties in P and beam flux typical of a single data set.

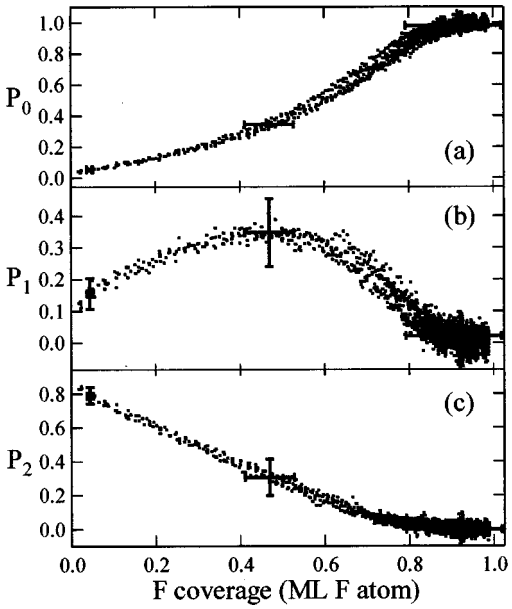

FIG. 13. Reaction probability of F_2 at $E_i=0.7$ kcal/mol with Si(100) at 250 K as a function of fluorine coverage for P_0 unreactive scattering, P_1 single atom abstraction, and P_2 two atom adsorption. Data from Fig. 12.

B. Coverage dependence of reaction probabilities

In the previous section, the absolute reaction probabilities were determined for scattering into a given detection angle, $P_0(\epsilon,\theta_d)$, $P_1(\epsilon,\theta_d)$ and $P_2(\epsilon,\theta_d)$. An additional result of interest is the absolute reaction probability integrated over all detector angles, both in-plane and out-of-plane, in the hemisphere above the surface to yield $P_0(\epsilon)$, $P_1(\epsilon)$ and $P_2(\epsilon)$. However, integration of the probabilities given in Eqs. (IV.8) and (IV.10) over detection angle is obviated by the independence of the scattered F_2 and F signals as a function of exposure on θ_d in the scattering plane, as shown in Figs. 5 and 6. Scattering of F_2 and F outside of the plane defined by the incident beam and the surface normal were not measured, but the independence of the reaction probabilities on the in-plane detector angle, θ_d, suggests that a dependence on the out-of-plane angle is physically unlikely. Moreover, the lack of dependence of the scattered F_2 and F signals as a function of exposure, and hence of the reaction probabilities as a function of exposure, on the azimuthal angle as shown in Fig. 7, indicates that there is no significant alignment effect in the exit channel of the reaction which would lead to preferential scattering of the product along specific crystal axes and hence to anisotropic out-of-plane scattering. There is other evidence for the isotropic nature of the interaction with and scattering from this highly corrugated Si surface. For example, the independence of the reaction probabilities on incident angle, as shown in Fig. 6, indicates that the reaction is nonactivated with no preferential incident angle of approach of the F_2 molecule into the entrance channel. In addition, the tremendous exothermicity released in this reaction overwhelms the low incident energy and any memory of the incident trajectory, leading to a near cosine dependence of the scattered product intensities on the angle from the surface normal, as discussed in the following section. Thus, the absolute reaction probability for low energy F_2 on Si(100) at 250 K is independent of the detection angle, i.e., $P(\epsilon)=P(\epsilon,\theta_d)$.

Having obtained $P_1(\epsilon)$ and $P_2(\epsilon)$, the probabilities for adsorption of one and two fluorine atoms, respectively, as a function of exposure, the fluorine coverage as a function of exposure can be now calculated. By definition of the probabilities, there will be P_1+2P_2 fluorine atoms adsorbed on the surface for each incoming F_2 molecule. Summing over all incoming F_2 molecules, the coverage, $\theta(\epsilon)$, can be written as

$$\theta(\epsilon)=\int_0^{\epsilon} I_{F_2}(0.5P_1(\epsilon)+P_2(\epsilon))d\epsilon, \qquad \text{(IV.11)}$$

where I_{F_2} is the incident F_2 flux in ML F/s. Figure 12(d) shows the absolute fluorine coverage as a function of F_2 exposure. The coverage rapidly increases from a low value at initial exposures to a saturation level of 0.94 ± 0.11 (95%, $N=9$) ML at exposures above 10 ML F atoms. This plot of the fluorine coverage as a function of exposure is then used to recast the probabilities in terms of coverage, $P_2(\theta)$, $P_1(\theta)$, and $P_0(\theta)$, presented in Fig. 13.

C. Saturation coverage and identification of abstraction and adsorption sites

The analysis in the previous section along with the saturation of the thermal desorption signal in Fig. 9 shows clearly that the abstraction reaction and the adsorption of F_2 on Si ceases at a coverage of 0.94 ± 0.11 (95%, $N=9$) ML. The cessation of atom abstraction and adsorption at this coverage leads to the conclusion that there are about 1 ML of

abstraction sites and 1 ML of adsorption sites on the Si(100) surface. As described in Sec. III B 3, the He diffraction measurements show that the saturated F overlayer has the same two-dimensional periodicity, (2×1), as the underlying Si(100) substrate. Given that adsorption of fluorine atoms on the dangling bonds would maintain the (2×1) periodicity, the observation of a (2×1) surface unit cell for the fluorine overlayer strongly suggests that the dangling bonds are the F atom adsorption sites. Therefore, because the number of dangling bond sites on this crystal, 1 ML, is the same as the number of adsorption and abstraction sites, it is concluded that not only are the dangling bonds the adsorption sites but that they are also the abstraction sites.

V. DISCUSSION

A picture of the interaction of low energy F_2 with Si(100) from zero to saturation coverage at 250 K is now at hand from these experimental results. The following section is divided into a discussion of the interaction at zero coverage and at higher coverages.

A. Phenomenological model at zero coverage

As a F_2 molecule approaches Si(100), it has almost a unity probability of undergoing an abstraction event, $1-P_0(\theta=0.02\,\text{ML})=0.957\pm0.003$ (95%, $N=9$), in which one of the fluorine atoms of the incident F_2 is abstracted by one of the dangling bonds and is then adsorbed at that dangling bond site. The complementary F atom is expelled rapidly as a result of the exothermicity of the reaction. It can fly into the gas phase where it is detected and contributes to the measurement of P_1 or it can adsorb onto the surface and contribute to the value of P_2. Only a minority of reactive trajectories, $P_1(\theta=0.02\,\text{ML})=0.13\pm0.03$ (95%, $N=9$), undergo single atom abstraction in which only one of the F atoms is adsorbed while the vast majority of them result in two atom adsorption, $P_2(\theta=0.02\,\text{ML})=0.83\pm0.03$ (95%, $N=9$). These results reflect deeply on the potential energy surface for the interaction of F_2 with Si(100), as now described.

1. Dynamics of F atom abstraction

The TOF measurements of the scattered F atoms presented in Figs. 1–3 provide dynamical information about the atom abstraction mechanism. As discussed in Sec. III, the scattered F atoms have a much faster velocity distribution than a thermal distribution characterized by the crystal temperature. This fast distribution arises from the reaction exothermicity which is channeled into the translational motion of the scattered F atom on a time scale that is rapid compared to that required for accommodation on the surface. However, while the velocity distribution is fast, it is not fast enough to account for all of the reaction exothermicity. The average energy of the F atoms is 3.7 ± 0.4 kcal/mol, only a few percent of the total reaction exothermicity of 103 kcal/mol.[30] The low translational energy of the products is consistent with an ''early barrier'' or ''attractive potential'' type of potential energy surface first described by Evans and Polanyi for gas phase reactions.[31] In the prototypical three atom reaction $A+B_2\rightarrow AB+B$, an ''attractive potential'' surface leads to low translational energy and high vibrational energy in the products AB and B. For the gas–surface case of F_2 on Si(100), the vibrational excitation is in the surface Si–F bond. For the case of the interaction of XeF_2 with Si, emission at about 1400 cm^{-1} has been attributed to the decay of such a vibrationally excited fluorinated Si surface species.[32]

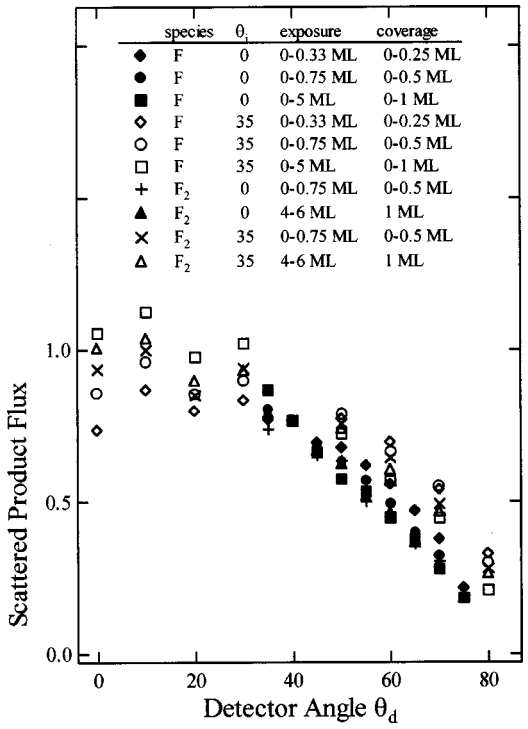

FIG. 14. Scattered F and F_2 flux as a function of θ_d at $\theta_i=0°$ and 35° for various exposures normalized to $\cos 40°$ at $\theta_d=40°$. The scattered flux is obtained by integrating data similar to those shown in Figs. 4–7 over indicated range of exposure in ML F atom. Coverage range is determined from Fig. 12(d).

Figure 14 shows angular distributions of the scattered F_2 (solid symbols) measured at both 0° and 35° incident angles and at both low fluorine coverages, from 0–0.25 and 0–0.5 ML, and at 1 ML saturation coverage. Figure 14 also shows the angular distributions of the scattered F atoms (open symbols) measured at both 0° and 35° incident angles and at both low and high coverages. The values of the scattered F_2 and F atom fluxes are derived from measurements such as shown in Figs. 5 and 6 after converting the F_2 exposure to fluorine coverage using data such as presented in Fig. 12(d). Each angular distribution has been normalized to the value of $\cos 40°$ at $\theta_d=40°$ for ease of comparison to each other.

The angular distributions of both the scattered F_2 molecules and the scattered F atoms are broad and depend on the cosine of the detection angle as measured from the surface normal. Given that the velocities of the scattered F_2 and F atoms are isotropic, that is, do not depend on the detection angle, a cosine dependence is expected. The cosine angular dependence for the scattered F atom regardless of incident angle and coverage is particularly interesting because it implies that the scattered F atom loses all memory of its incident trajectory. This observation suggests that the transition state for atom abstraction is ''loose,'' meaning that it is not geometrically constrained by approach geometry or steric

hindrance. This experimental observation is in disagreement with molecular dynamics simulations[12] that show the F_2 molecule aligning itself with the dangling bond prior to its dissociation. This late transition state along the reaction coordinate leads to other results from the simulations that are contradictory to experiment such as the branching between two atom adsorption and single atom abstraction, as discussed further below.

2. Reactivity at zero coverage and comparison to previous work

The total reaction probability of F_2 with Si(100), P_{total}, is defined in this work as the sum of the probabilities for single atom abstraction and two atom adsorption, $P_{\text{total}}=P_1+P_2$. This definition is equivalent to what other authors[7] have called the apparent sticking coefficient, S_{app}. Still other authors[6] have defined the reaction probability of F_2 with Si(100) as the probability of a F atom sticking to the surface, labeled as the true sticking coefficient, S_{true}. The true sticking coefficient is related to the values of P_1 and P_2 in this investigation as a weighted average, $S_{\text{true}}=0.5P_1+P_2$. For the sake of comparison to previous work, the results of this investigation yield values of $S_{\text{app}}=0.96\pm0.04$ and $S_{\text{true}}=0.90\pm0.04$ for the apparent and true initial sticking coefficients, respectively, at zero coverage. The small difference in these two values arises from the low probability for single atom abstraction, P_1.

Engel *et al.*[6] obtain $S_{\text{true}}=0.46\pm0.02$ for F_2 on Si(100) at temperatures between 120 to 600 K and at zero coverage by evaluating the initial slope of a plot of the fluorine coverage, measured by x-ray photoelectron spectroscopy (XPS), versus exposure. This value for S_{true} is only half the value measured in the present study. The most probable cause of this discrepancy is the extreme grazing incidence, $\theta_i=75°$, mandated by geometric constraints of their apparatus, as compared to normal incidence used here. Shadowing effects have been observed in the present study at extreme grazing incidence. These effects, which likely arise from the strong corrugation of the covalently bonded Si surface, are consistent with lower sticking coefficients. Note that this method for measuring the sticking coefficient or reaction probability cannot distinguish between fluorine adsorbed as a result of single atom abstraction and fluorine adsorbed as a result of two atom adsorption.

Kummel *et al.* report values for S_{app} ranging from $\sim$0.57 at a low incident energy ($\sim$1.4 kcal/mol) to $\sim$0.90 at high incident energy for F_2 on Si(100) at 300 K.[7] To facilitate a comparison to this previous work, measurements were made at $E_i=1.5$ kcal/mol. The results show that S_{app} remains constant at 0.90 for incident energies between 0.7 to 1.5 kcal/mol. Therefore, the present value for the total reaction probability at zero coverage, or equivalently, $S_{\text{app}}=0.96\pm0.04$, is larger than that measured by Kummel, $S_{\text{app}}=\sim0.57$. Unlike the present investigation in which the loss of both F_2 flux and the appearance of F atoms is measured directly with a differentially pumped mass spectrometer, Kummel *et al.*[7] measure the decrease in the background partial pressure of F_2 in the main chamber where the crystal is housed.[33] This decrease is assumed to be proportional to the decrease in the scattered F_2 flux due to its adsorption on the crystal. As shown in Sec. III B 2, this assumption is not valid in the case of desorption of radical species, a process which is clearly taking place during the atom abstraction reaction of F_2 with Si. While they are cognizant that the decrease in the F_2 background partial pressure reflects not only the reaction of F_2 with the Si crystal but also with the vacuum chamber walls, they are unable to determine directly the effect of the wall reactions on their measurement. Instead, they derive the wall reactivity by reconciling their value of S_{app} with the value of S_{true} of Engel *et al.*[6] Of course, this reconciliation assumes that it is appropriate to compare the two measurements. Considering the extreme grazing incidence used in the study of Engel *et al.* and the normal incidence of the work of Kummel *et al.*, this procedure for evaluating the wall reactivity is probably not appropriate. As with the method used by Engel *et al.*, the method of Kummel *et al.* cannot distinguish between single atom abstraction and two atom adsorption.

The molecular dynamics simulations by Carter *et al.*[12] yield a value of $S_{\text{true}}=0.59$ for a low incident energy, 0.7 kcal/mol, of F_2 on Si(100) at zero coverage. However, their calculated value for the total reaction probability is nearly unity, $S_{\text{app}}=0.99$, in agreement with the experimental results presented here. The dramatic difference between S_{app} and S_{true} as calculated in the simulations arises because of the high probability for single atom abstraction.

3. Single atom abstraction versus two atom adsorption at zero coverage

Given that the atom abstraction mechanism was not detected in either of the two previous experimental studies of the interaction of F_2 with Si(100), no comparisons of the branching ratio between the two dissociative chemisorption channels, single atom abstraction and two atom adsorption, can be made with previous experimental work. However, comparisons made with the branching ratio calculated in molecular dynamics simulations by Carter *et al.*[12] reveal major discrepancies. The simulations find that single atom abstraction is the dominant mechanism for dissociative chemisorption at low incident energy. The calculated values of $P_1=0.81$ and $P_2=0.19$ for single atom abstraction and two atom adsorption, respectively, are in stark contrast to the experimental values of $P_1=0.13\pm0.03$ and $P_2=0.83\pm0.03$. Steps and defects were initially speculated as the source of the discrepancy between experiment and theory, but subsequent simulations showed no dependence of the reactivity on step or defect density.[13]

The disagreement between the experiment and the simulations extends beyond the absolute values of the reaction probabilities and points to the WWC potential as an inaccurate representation of the interaction between F_2 and Si. For example, the calculated average scattered F atom velocity of $\sim$2000 m/s[12] is almost double the value of 1084 ± 46 m/s measured in this experiment. This overestimation of the escape velocity underestimates both the time that a F atom spends near the surface as well as the forces it feels. Thus, the WWC potential[11] underrates the coupling of the $Si-F_2$ transition state to the rest of the Si lattice causing a much higher fraction of the exothermicity to be channeled into the

translational energy of the scattered F atom and leading in turn to a value for P_2 that is too low compared to the experimental one. In addition, the calculated angular distributions of the scattered F atoms are peaked about the Si–F bond direction.[12] Carter *et al.*[12] argue that this alignment precludes the scattered, complementary F atom from adsorbing on the surface and thereby from contributing to the value of P_2. In contrast to the calculated angular distributions, this experiment reveals the scattered F atom angular distribution to be essentially isotropic, as shown in Fig. 14.

Kummel *et al.*[34] interpret their STM studies of F_2 on Si(111) to be in agreement with the theoretical work of Carter for F_2 on Si(100).[12] In the low coverage limit, they interpret F atoms adsorbed without neighboring F atoms to arise solely from single atom abstraction, thereby contributing to P_1, and F atoms adsorbed close to each other as a pair to arise solely from two atom adsorption, thereby contributing to P_2. With the aid of a Monte Carlo simulation to reproduce their results, they conclude that all reactions must occur via single atom abstraction at low incident energy. In addition, they observe an incident energy dependence similar to that of Carter, in which P_2 increases at the expense of P_1 with increasing E_i. However, using STM as the sole method to deduce gas–surface reaction dynamics is questionable. Given that the thermodynamics of atom abstraction does not necessitate that the complementary F atom of a P_2 trajectory be bound at the site immediately adjacent to the initial abstraction site, it is highly speculative to distinguish between single atom abstraction and two atom adsorption based on a spatial distribution of adsorbates. This issue is discussed in more detail in Sec. V C.

B. Interaction of low energy F_2 with fluorinated Si(100) at 250 K

As the fluorine coverage increases from zero to about 0.5 ML, P_2 decreases almost linearly with coverage from 0.83 ± 0.03 to 0.31 ± 0.08 (95%, $N=9$). In contrast, P_1 approaches a maximum of 0.35 ± 0.08 (95%, $N=9$) at about 0.5 ML. Beyond 0.5 ML, both reactive channels decay, approaching zero at 0.94 ± 0.11 ML, the coverage at which all of the dangling bonds are fluorinated and the Si surface is passivated to further reaction with F_2. The saturated overlayer is well ordered and exhibits a (2×1) surface periodicity. There is no evidence for the cleavage of lattice bonds between the Si surface atoms or between the first and second layer Si atoms. The unusual coverage dependence of both reactive channels can be described by a statistical model that is presented and discussed in an accompanying paper.[15]

A previous study of the saturation coverage in this system does not agree with the present results. Using XPS to monitor the adsorbed fluorine, Engel *et al.*[6] measured the exposure dependence of the absolute fluorine coverage and determined an initially fast rate of adsorption up to a saturation coverage of 1.5 ML, followed by a much slower rate of adsorption that lead to a coverage of 3–4 ML after very long exposures. They attribute the initial fast adsorption to reaction with the dangling bonds, but do not explain the shortage of dangling bond adsorption sites needed to attain 1.5 ML. Unfortunately, no complementary techniques such as diffraction were used to corroborate the results of these XPS measurements. In contrast, the present experimental results are consistent with the results from molecular dynamics simulations which suggest that the saturation coverage of low energy F_2 on Si(100) is 1.0 ML and that no reaction of low energy F_2 occurs at 1 ML.[12]

An important result from the present experimental studies is the observation that the exothermicity of the reaction of F_2 with Si is not a source of lattice disorder. This observation is in contrast to experimental and theoretical works that have suggested that the disorder of the Si lattice induced by local heating due to the large amount of energy released in the adsorption process initiates etching.[11,12,35] For example, Carter *et al.* initially suggested that the heat of adsorption for F atoms on Si(100) leads to the dissociation of SiF_2 groups that diffuse along the surface and inevitably lead to lattice disorder.[11,12] Subsequent simulations agreed with this suggestion, but restricted disorder only for F atoms with incident translational energies above 2.5 eV.[36] Lattice disorder may be a requisite for etching and, indeed, the absence of F_2 etching in this system with no disorder is consistent with this requirement. However, it is clear that disorder at coverages of 1 ML and less does not arise from the reaction exothermicity of F–Si bond formation, which is considerable at 103 kcal/mol. In fact, F atoms and XeF_2 reactions with Si(100) have similar exothermicities, about 141 and 86 kcal/mol, yet both are excellent etchants. Thus, it is unlikely that the reaction exothermicity, by virtue of providing lattice disorder, is the primary explanation for etching.

C. Atom abstraction in other gas–surface systems

Atom abstraction is not unique to the F_2/Si system. If the energy released in forming one surface–adsorbate bond is sufficient to compensate for the energy required to break the bond of the incident molecule, then abstraction by the surface is possible. An interesting candidate for atom abstraction is the interaction of O_2 with Al(111), although the observation of isolated adsorbed atomic oxygen atoms on Al(111) using STM[37] has been interpreted as evidence for hot atom motion of the two atoms resulting from a classic dissociative chemisorption event. Hot atom motion arises from the release of the exothermicity into parallel translational motion of the two atoms away from each other.[38–40] The atoms remain bound to the surface but travel along the surface until they dissipate enough energy to be trapped at a chemisorption site. Although this interpretation is plausible, especially considering subsequent work on O_2 on Pt(111)[41] and on Ag(110)[42] where two atom adsorption is energetically required, the results can also be explained by oxygen atom abstraction.[2,43] Unfortunately, the use of STM as the sole probe of dynamics of such a fast nature inevitably leads to ambiguity because the end result of each mechanism is likely to be indistinguishable. Both atom abstraction and hot atom motion are dissociative chemisorption processes in which the two fragments separate from each other and lead independent existences. However, in hot atom motion, which arises from classic dissociative chemisorption, both atoms are and remain bound to the surface during their horizontal motion because the exothermicity is insufficient to allow one or both

to escape from the surface. In contrast, the complementary atom in atom abstraction is not initially bound to the surface and may move parallel to the surface for some distance before encountering an adsorption site. In either case, the hot atom or the abstracted atom will likely appear to a STM observation at some distance from its partner.

Earlier work on other gas–surface systems shows evidence consistent with atom abstraction. Lunsford *et al.* observed CH_3 production upon passing methane over a MgO surface[44] implying H atom abstraction by the MgO surface. White *et al.* observed CH_3 production upon adsorption of methyl bromide on a potassium doped Ag surface.[45] Bent *et al.* reported CH_3 production upon thermal desorption of molecularly adsorbed CH_3I from a Cu surface.[46] Selective I atom abstraction in the ICI[47] system probed by STM and chlorine atom abstraction in the Cl_2/K system[48] have been suggested to occur.

As noted in the Introduction, atom abstraction may have dramatic effects in semiconductor etching because the scattered reaction product is an extremely reactive open shell atom or radical. For example, in the semiconductor industry, the constant desire for smaller and smaller features requires the ability to selectively etch the semiconductor surface with precision. However, a major problem in the dry etching of semiconductors is a phenomenon called undercutting in which etching occurs under the resist. This may be caused, in part, by radicals produced by atom abstraction. Thus, the inhibition of atom abstraction could prevent undercutting.

An example of atom abstraction during a semiconductor etching reaction is that of XeF_2 on Si. Recent work by Ceyer *et al.* has shown direct evidence for F atom abstraction in the XeF_2/Si(100) system.[49] Once again, TOF techniques are used to distinguish between unreactively scattered XeF_2 and XeF arising from atom abstraction. The important point here is that atom abstraction occurs during the steady state reaction in which XeF_2 efficiently etches Si(100) at 250 K and that it is not just a minor channel only present at low coverages on smooth surfaces. Atom abstraction may be particularly prevalent in semiconductor chemistry because dangling bonds provide extremely reactive sites for the abstraction event by virtue of not involving the cleavage of lattice bonds. Nevertheless, the production of very reactive species in the gas phase arising from atom abstraction in heterogeneous catalytic or chemical vapor deposition systems may also have profound effects, either very useful or detrimental, to the specific chemical process. Atom abstraction potentially has significant implications for many chemical processes at interfaces.

VI. CONCLUSIONS

The Si(100)2×1 surface abstracts a F atom from an incident, low energy F_2 molecule while the reaction exothermicity propels the complementary F atom back into the gas phase. The broad angular distribution and low average translational energy, relative to the available reaction exothermicity, of the scattered F atoms indicate a ''loose'' transition state positioned in the entrance channel of the reaction coordinate. It is concluded that the Si dangling bonds are responsible for the abstraction process and are also the sites for adsorption. No Si–Si lattice bonds are observed to be cleaved upon the interaction of F_2 with Si(100). Once one fluorine atom is bound to each of the dangling bonds, thereby forming an overlayer of (2×1) periodicity and of 1 ML coverage, the adsorption of F_2 ceases. Although the complementary F atom can scatter back into the gas phase, it does not necessarily do so. If the complementary F atom has some parallel component to its outgoing trajectory, it may be caught by an adjacent or nearby dangling bond and adsorb there in a process called two atom adsorption. The probability for two atom adsorption decreases with coverage while the probability for single atom abstraction exhibits a non-Langmuirian behavior in which a maximum is observed at about 0.5 ML. A simple model based on lattice gas kinetics has been developed to understand this peculiar coverage dependence and is presented in an accompanying paper.[15] Briefly, it allows the chemistry of those incident F_2 molecules whose axes are roughly parallel to the surface to be distinguished from those that are vertical. Its good agreement with the data indicates that the mechanism for dissociative chemisorption indeed proceeds as a two step process involving first an abstraction step followed by the adsorption of the second F atom if it is propelled across the surface in the direction of an empty dangling bond.

ACKNOWLEDGMENTS

M.R.T., K.B.L., and S.C.E. gratefully acknowledge the support of DOD through a NDSEG-ONR Predoctoral Fellowship, the National Science Foundation (NSF) through a Postdoctoral Research Fellowship and the NSF through a Predoctoral Fellowship, respectively. This work is supported by NSF CHE-9713276.

[1] D. D. Eley and E. K. Rideal, Nature (London) **146**, 401 (1940); Proc. R. Soc. London, Ser. A **178**, 429 (1941); D. D. Eley, *ibid.* **178**, 452 (1941).
[2] Y. L. Li, D. P. Pullman, J. J. Yang *et al.*, Phys. Rev. Lett. **74**, 2603 (1995); S. T. Ceyer, *Proc. R. A. Welch Found. Conf. Chem. Res. XXXVIII: Chemical Dynamics of Transient Species* (Welch Foundation, Houston, 1994), pp. 156–172; D. P. Pullman and S. T. Ceyer, Abstracts of Am. Chem. Soc. **207**, 168 (1994).
[3] H. F. Winters and J. W. Coburn, Surf. Sci. Rep. **14**, 161 (1992).
[4] M. L. Yu and L. A. DeLouise, Surf. Sci. Rep. **19**, 285 (1994).
[5] J. R. Engstrom, M. M. Nelson, and T. Engel, Phys. Rev. B **37**, 6563 (1988).
[6] J. R. Engstrom, M. M. Nelson, and T. Engel, Surf. Sci. **215**, 437 (1989).
[7] E. R. Behringer, H. C. Flaum, D. J. Sullivan, D. P. Masson, E. J. Lanzendorf, and A. C. Kummel, J. Phys. Chem. **99**, 12863 (1995).
[8] E. W. Kuipers, A. Vardi, A. Danon, and A. Amirav, Phys. Rev. Lett. **66**, 116 (1991).
[9] C. T. Rettner, Phys. Rev. Lett. **69**, 383 (1992).
[10] F. H. Stillinger and T. A. Weber, Phys. Rev. Lett. **62**, 2144 (1989); T. A. Weber and F. H. Stillinger, J. Chem. Phys. **92**, 6239 (1990).
[11] C. J. Wu and E. A. Carter, Phys. Rev. B **45**, 9065 (1992); P. C. Weakliem, C. J. Wu, and E. A. Carter, Phys. Rev. Lett. **69**, 200 (1992); P. C. Weakliem and E. A. Carter, J. Chem. Phys. **98**, 737 (1993).
[12] L. E. Carter, S. Khodabandeh, P. C. Weakliem, and E. A. Carter, J. Chem. Phys. **100**, 2277 (1994); L. E. Carter and E. A. Carter, J. Phys. Chem. **100**, 873 (1996).
[13] L. E. Carter and E. A. Carter, J. Vac. Sci. Technol. A **12**, 2235 (1994); L. E. Carter and E. A. Carter, Surf. Sci. **323**, 39 (1995).
[14] T. A. Schoolcraft and B. J. Garrison, J. Vac. Sci. Technol. A **8**, 3496 (1990); T. A. Schoolcraft, A. M. Diehl, A. B. Steel, and B. J. Garrison, *ibid.* **13**, 1861 (1995).
[15] M. R. Tate, D. P. Pullman, D. Gosalvez-Blanco, A. A. Tsekouras, Y. L. Li, and S. T. Ceyer, J. Chem. Phys. (submitted).

[16] S. T. Ceyer, D. J. Gladstone, M. McGonigal, and M. T. Schulberg, *Physical Methods of Chemistry*, edited by B. W. Rossiter and R. C. Baetzold, 2nd ed. (Wiley, New York, 1993), Vol. IXA, p. 383.
[17] D. Gosalvez-Blanco, Ph.D. thesis, Massachusetts Institute of Technology, 1997.
[18] D. R. Miller, *Atomic and Molecular Beam Sources*, edited by G. Scoles (Oxford University Press, New York, 1988).
[19] P. K. Sharma, E. L. Knuth, and W. S. Young, J. Chem. Phys. **64**, 4345 (1976).
[20] V. H. Reis and J. B. Fenn, J. Chem. Phys. **39**, 3240 (1963).
[21] A. Ishizaka and Y. Shiraki, J. Electrochem. Soc. **133**, 666 (1986).
[22] H. C. Straub, P. Renault, B. G. Lindsay, K. A. Smith, and R. F. Stebbings, Phys. Rev. A **52**, 1115 (1995).
[23] Commission on Atomic Weights and Isotopic Abundances, ''Table of isotopic compositions of the elements as determined by mass spectrometry,'' 1989.
[24] F. A. Stevie and M. J. Vasile, J. Chem. Phys. **74**, 5106 (1981).
[25] H. C. Straub and K. A. Smith (private communication).
[26] M. J. Cardillo and G. E. Becker, Phys. Rev. B **21**, 1497 (1980).
[27] H. F. Winters and F. A. Houle, J. Appl. Phys. **54**, 1218 (1983).
[28] J. J. Yang, Ph.D. thesis, Massachusetts Institute of Technology, 1993.
[29] T. R. Hayes, R. C. Wetzel, and R. S. Freund, Phys. Rev. A **35**, 578 (1987).
[30] Using a calculated value of 148 kcal/mol for Si–F bond energy [C. J. Wu *et al.*, J. Am. Chem. Soc. **113**, 9061 (1991)], 7 kcal/mol for π bond energy of Si dimers [M. P. D'Evelyn *et al.*, J. Chem. Phys. **96**, 852 (1992); U. Hofer *et al.*, Phys. Rev. B **45**, 9485 (1992)] and 38 kcal/mol for F_2 bond energy, exothermicity is estimated to be 103 kcal/mol.
[31] M. G. Evans and M. C. Polanyi, Trans. Faraday Soc. **35**, 178 (1939).
[32] T. J. Chuang, Phys. Rev. Lett. **42**, 815 (1979).
[33] D. A. King and M. G. Wells, Surf. Sci. **29**, 454 (1972).
[34] J. A. Jensen, C. Yan, and A. C. Kummel, Science **267**, 493 (1995).
[35] C. W. Lo, P. R. Varekamp, D. K. Shuh, T. D. Durbin, V. Chakarian, and J. A. Yarmoff, Surf. Sci. **292**, 171 (1993).
[36] L. E. Carter and E. A. Carter, Surf. Sci. **360**, 200 (1996).
[37] H. Brune, J. Wintterlin, R. J. Behm, and G. Ertl, Phys. Rev. Lett. **68**, 624 (1992); H. Brune, J. Wintterlin, J. Trost, G. Ertl, J. Wiechers, and R. J. Behm, J. Chem. Phys. **99**, 2128 (1993).
[38] B. Kasemo and J. Harris, Surf. Sci. **105**, L281 (1981).
[39] S. Caratzoulas, B. Jackson, and M. Persson, J. Chem. Phys. **107**, 6420 (1997); D. Shalashilin and B. Jackson, *ibid.* **109**, 2856 (1998).
[40] S. L. Tang, J. D. Beckerle, M. B. Lee, and S. T. Ceyer, J. Chem. Phys. **84**, 6488 (1986).
[41] J. Wintterlin, R. Schuster, and G. Ertl, Phys. Rev. Lett. **77**, 123 (1996).
[42] J. V. Barth, T. Zambelli, J. Wintterlin, and G. Ertl, Chem. Phys. Lett. **270**, 152 (1997).
[43] L. Österland, I. Zoric, and B. Kasemo, Phys. Rev. B **55**, 15452 (1997).
[44] D. J. Driscoll, W. Martir, J. X. Wang, and J. H. Lunsford, J. Am. Chem. Soc. **107**, 58 (1985).
[45] X. L. Zhou, S. R. Coon, and J. M. White, J. Chem. Phys. **94**, 1613 (1991).
[46] J. L. Lin and B. E. Bent, J. Am. Chem. Soc. **115**, 2849 (1993); P. W. Kash, D. H. Sun, M. Xi, G. W. Flynn, and B. E. Bent, J. Phys. Chem. **100**, 16621 (1996).
[47] Y. Liu, D. P. Masson, and A. C. Kummel, Science **276**, 1681 (1997).
[48] J. Strömquist, L. Hellberg, B. Kasemo, and B. I. Lundqvist, Surf. Sci. **352**, 435 (1996).
[49] S. T. Ceyer and co-workers, to be published.